Deformation of a flexible fiber in a viscous flow past an obstacle

H. M. López, J.-P. Hulin, H. Auradou, and M. V. D'Angelo

Citation: Physics of Fluids (1994-present) **27**, 013102 (2015); doi: 10.1063/1.4905920
View online: http://dx.doi.org/10.1063/1.4905920
View Table of Contents: http://scitation.aip.org/content/aip/journal/pof2/27/1?ver=pdfcov
Published by the AIP Publishing

PHYSICS OF FLUIDS **27**, 013102 (2015)

Deformation of a flexible fiber in a viscous flow past an obstacle

H. M. López,[1,a)] J.-P. Hulin,[2,b)] H. Auradou,[2,c)] and M. V. D'Angelo[1,d)]
[1]*Grupo de Medios Porosos, Facultad de Ingeniería, CONICET, Paseo Colon 850, 1063 Buenos Aires, Argentina*
[2]*University Paris-Sud, CNRS, F-91405. Laboratory FAST, Bât 502, Campus University, Orsay F-91405, France*

(Received 4 August 2014; accepted 29 December 2014; published online 20 January 2015)

We study the deformation and transport of elastic fibers in a viscous Hele-Shaw flow with curved streamlines. The variations of the global velocity and orientation of the fiber follow closely those of the local flow velocity. The ratios of the curvatures of the fibers by the corresponding curvatures of the streamlines reflect a balance between elastic and viscous forces: this ratio is shown experimentally to be determined by a dimensionless *Sperm number Sp* combining the characteristic parameters of the flow (transverse velocity gradient, viscosity, fiber diameter/cell gap ratio) and those of the fiber (diameter, effective length, Young's modulus). For short fibers, the effective length is that of the fiber; for long ones, it is equal to the transverse characteristic length of the flow. For $Sp \lesssim 250$, the ratio of the curvatures increases linearly with Sp; for $Sp \gtrsim 250$, the fiber reaches the same curvature as the streamlines. © *2015 AIP Publishing LLC.* [http://dx.doi.org/10.1063/1.4905920]

I. INTRODUCTION

The transport of flexible biological or man made fibers by a flow and their deformation is of interest in view of their potential applications in many different industrial fields. A first example is the paper industry in which the orientation and spatial distributions of the fibers in the flowing pulp must be controlled.[1,2] Fibers are also widely used by petroleum engineers[3] to enhance the proppant transport capabilities of fracturing fluids, or to prevent the backflow of proppant. Other domains of application are civil engineering (special cements, structural reinforcement), textile engineering, bio engineering and medicine.

In flows at low Reynolds numbers, the deformation of fibers reflects a balance between viscous and elastic stresses and plays often an important part: for instance, these effects are critical for understanding the dynamics of flexible biological filaments,[4–6] the filtration and cross stream migration of macromolecules in small channels,[7–10] and the positioning of bio-fibers in porous media.[11] In all these applications, the prediction of the motion of the fibers is a difficult fundamental problem, particularly in complex geometries and inhomogeneous flows where constrictions and obstacles are present: these create complex interactions between the flexible objects, the flowing fluids, and the solid walls.

Our interest in these problems is focused on the injectability and transport of long flexible fibers through fractures in reservoir rocks. In a previous work,[12] we studied fiber transport by a flow in single narrow model rough fractures and of its dependence on the fluid velocity, the flexibility of the fiber, and the configuration of the aperture field.

The present work is devoted to a quantitative study of the influence of the parameters in the configuration where the fiber passes in the vicinity of contact areas or close to regions of low aperture.

a)Electronic mail: lopezhmatias@gmail.com
b)Electronic mail: hulin@fast.u-psud.fr
c)Electronic mail: Harold.Auradou@u-psud.fr
d)Electronic mail: veronica.dangelo@gmail.com

This situation is modeled experimentally by means of a Hele-Shaw cell of constant aperture and of width varying with the distance: this allows one to determine the variations along the flow of the orientation and deformation of the flow lines and of a fiber placed in the flow. More specifically, we seek to relate the variations of the curvature of the fiber to those of the streamlines, to the velocity gradients, and to the geometrical and mechanical properties of the fiber.

Most past studies considered the simpler case of flexible fibers in a nonconfined parallel shear flow[13–16] of shear rate $(\partial v/\partial n)$ (v is the modulus of the local flow velocity and the derivative is taken is the direction perpendicular to the flow lines). In such a configuration, the fiber may rotate about its axis and buckles above a threshold value of the Sperm number which characterizes the relative magnitudes of the viscous and elastic forces and is equal to

$$\frac{\mu(\partial v/\partial n)\xi^4}{EI}; \tag{1}$$

μ is the viscosity, $(\partial v/\partial n)$ is the shear rate along the fiber, E its Young's modulus, I its area moment of inertia ($I = \pi D^4/64$ for a circular cross section of diameter D), and ξ a characteristic dimension (for instance, the length L_f of the fiber). Other studies dealt with the cross stream migration of a flexible fiber in a parallel Poiseuille flow which is also strongly influenced by buckling.[8–10] Finally, buckling is also observed above a critical value $Sp \sim 120$[17] of Sp for fibers approaching a stagnation point.[18–20] Numerically, slender-body theory has been used to model the behavior of an elastic fiber (with one clamped end) in the vicinity of a corner in a curved channel.[21] In this latter work, the variation with time and the final shape of the filament were analyzed in different corner geometries as a function of Sp. Recently, Wexler *et al.*[22] considered a fiber with one clamped end and initially transverse to a flow confined between two plates (like in the present case). In all cases, bending results from the combined effects of the hydrodynamic and viscous forces on the fibers: yet, in Refs. 21 and 22, their resultant is balanced by a force on the attachment point while, in the present case of a free fiber, this resultant must be zero, leading to very different shapes of the fibers.

In the following, we characterize first the flow field in the Hele-Shaw cell of varying width by means of dye tracer measurements and of $3D$ numerical simulations: we study, in particular, the variations of the velocity along the streamlines. Then, the local velocity and mean orientation of the fibers are compared to those of the fluid velocity at the same location. The curvature κ_f of the fibers is characterized by its ratio κ_f/κ_s to that of the streamlines: the variations of the extremal values of this ratio on different streamlines are studied as a function of the diameter D and length L_f of the fiber, of its initial transverse location, and of the flow velocity. The definition of the Sperm number Sp of the problem allowing one to take into account the influence of these different parameters is then discussed and the experimental dependence of κ_f/κ_s on Sp is analyzed.

II. EXPERIMENTAL PROCEDURE

The experimental setup consists of a Hele Shaw cell placed vertically. Its height and gap are, respectively, $L = 280$ and $H = 2.2 \pm 0.1$ mm (Fig. 1). The upper part of the cell has a Y-shaped section; the top is attached to a fluid bath with a slit at the bottom allowing for the flow of the fluid and the injection of the fibers. The fiber is injected in a funnel-shaped device which permits to select conveniently the location at which the fiber is injected. A rounded off step is then cut out of a transparent mylar sheet of thickness equal to H and inserted in the Hele Shaw cell. The mylar is tightly fitted so that no flow is observable between its surface and the walls of the cell. The height ΔW of the step parallel to the y axis is 30 mm and it is located in the middle of the cell; the width $W(x)$ of the flow section in the cell is then 70 mm in the inlet section and is reduced to 40 mm at the outlet as shown in the figure. The axis $y = 0$ corresponds to the boundary of the mylar sheet at the inlet.

Using a continuous rather than an abrupt variation of the height of the step boundary with the distance first minimizes unwanted solid-solid interactions between the fiber and this boundary. Moreover, a continuous variation of the width of the flow channel with distance is closer to the variation encountered in a real fractured rock. Finally, putting uniform flow sections before and after the step allows one to detect possible irreversible rotations and deformations of the fiber.

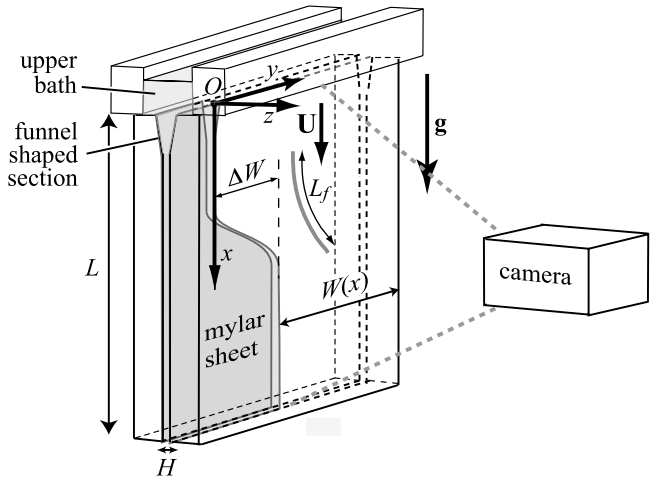

FIG. 1. Experimental setup.

A gear pump produces a downward flow; two Newtonian fluids are used: pure (MilliQ) water, of density $\rho = 997 \pm 1$ kg m^{-3} and a viscosity $\mu \approx 1$ mPa s, and a solution of 70% glycerol by weight in water, of density $\rho = 1178 \pm 1$ kg m^{-3} and viscosity $\mu \approx 15$ mPa s (27 °C). The flow rate Q is in the range of $10^4 \leq Q \leq 2.3 \times 10^4$ mm^3 s^{-1}, which corresponds to a characteristic velocity $95 \leq U \leq 230$ mm s^{-1}; in this work, U is the maximum of the Poiseuille velocity profile (half way between the walls) in the inlet parallel flow section upstream of the step. Downstream of the step, the velocity is higher by a factor of 1.75. For the water-glycerol solution, the corresponding Reynolds number $Re = UH/\nu$ is in the range of $16 \leq Re = UH/\nu \leq 40$. For water, one has, respectively, $210 \leq Re \leq 500$.

The flexible silicone fibers are made using a technique developed in the laboratory. Silicone is forced out of a syringe at an adjustable flow rate by means of a syringe pump. A second pump with a plate attached to the top is placed below the end of the first one so that the plate moves perpendicular to the flow. The injection leaves on the top of the plate thin flexible silicone fibers of constant diameter. The respective values of the speeds of the silicone at the outlet of the syringe pump and of the moving plate are very important. In order to obtain fibers of constant diameter, the velocity of the outflow must match approximately with that of the plate. If the speeds are not well matched, either the stream of silicone buckles or it breaks.[23] Fibers of different diameters can be made by using nozzles of different sizes: in the present work, nozzles of diameter 300–600 μm were used. The average D of the diameter over its orientation in the section and the fiber length is constant within ±0.015 mm from a fiber to another; the diameter is constant along the length for a given orientation within ±0.05 mm ($D = 0.49$ mm) and ±0.025 mm ($D = 0.49$ mm). In a given section, the variation of the diameter with its orientation is of the order of ±0.15 mm for $D = 0.91$ mm and ±0.02 mm for $D = 0.49$ mm. Large fibers become indeed elliptical because they sag under gravity before they polymerize: this effect is prevented by surface tension for $D \lesssim 0.7$ mm.

The lengths of the fibers are $L_f = 15$, 30, and 60 mm and, although they are lighter than water ($\rho_f = 796$ kg m^{-3}), the tests showed that gravity has little effect on the experimental results. In order to evaluate the stability of their properties, the silicone fibers were left overnight in different fluids (water and water glycerol solutions): no swelling occurred.

In the interpretation of the present experiments, the bending stiffness EI of the fiber plays a major role. In order to measure EI, the fiber is allowed to bend under its own weight with one of its ends clamped in a chuck-like device which keeps it locally horizontal; the fiber is placed in front of a dark background in order to achieve a high optical contrast. The process is repeated for several fiber lengths: $5 \leq L_f \leq 80$ mm. The values of δx, i.e., the vertical deflection of the tip of the fiber with respect to its position or a zero external load, and of L_f are determined with an uncertainty of ±20 μm by means of an image analysis technique developed by Semin *et al.*[24] In the present

TABLE I. Physical and mechanical characteristics of the fibers (D, ρ, and EI are, respectively, the diameter (averaged over the length of the fibers and the orientation in a section), the density, and the bending stiffness of the fiber).

Fiber	Material	D (mm)	ρ (kg m^{-3})	$EI \times 10^{-8}$ (N m^2)
$F1$	Silicone	0.49 ± 0.015	0.8	0.28 ± 0.04
$F2$	Silicone	0.91 ± 0.015	0.8	0.37 ± 0.04

case of a rod bent under its own weight and clamped at one end, the theoretical expression of δx is $m_L g L_f^4/(8EI)$ where $m_L g$ is the force per unit length (i.e., the weight per unit length). The data were analyzed by plotting the deflection δx as a function of the fourth power L^4 of the length. The relationship between these two quantities is linear for $\delta x/L \lesssim 0.1$; this is the limit of the small deflection approximation. The slope of this plot gives the value of EI (see Table I).

Experimentally, after the flow is established, the fibers are inserted into the upper inlet with one of the ends held by pliers. Three insertion points corresponding to different distances y_{inlet} from the boundary of the step at the inlet have been selected (see Fig. 2(a)). Once the fiber is aligned with the flow, it is released and digital images of its subsequent motion in the cell are recorded. In order to improve the contrast, the model is illuminated from behind by a plane light panel, and images are obtained by means of a digital camera at a rate of 30 fps and with a resolution of 1024×768 pixels (with 1 pixel = 0.22 mm). Each picture is then processed digitally in order to determine the instantaneous profile of the fibers.

The velocity of the fiber is determined from the displacement of its geometrical center between two consecutive pictures. The deformation of the fiber is characterized quantitatively by adjusting locally the profile by a polynomial function in order to determine the local slope and the curvature. Only experiments in which fibers are relatively straight and parallel to the flow before reaching the step were considered in the analysis.

In parallel with these experiments, three dimensional numerical simulations solving the full Navier-Stokes equation by means of the FLUENT™ package have also been carried out. These simulations provide both the components of the velocity and their derivatives with respect to the coordinates x, y, and z. The curvature of the streamlines and the derivative $\partial v/\partial n$ of the velocity with respect to distance perpendicular to these lines are then computed by combining the values of these derivatives.

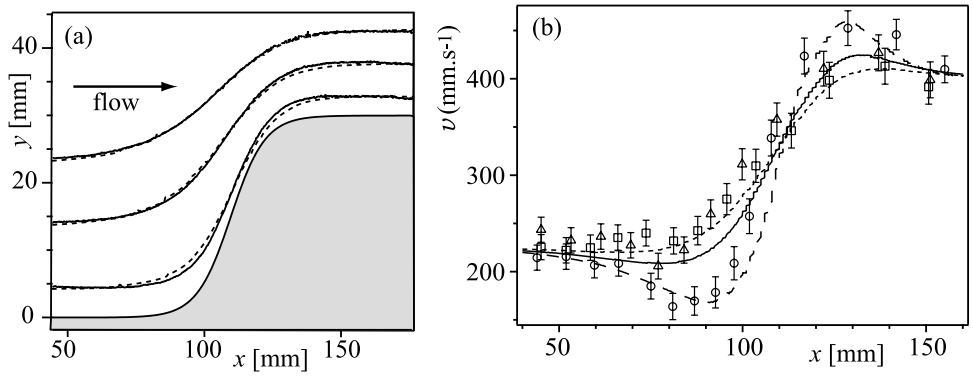

FIG. 2. (a) Visualization of three streamlines by the injection of a dye (continuous lines). Gray region: step obstacle; dotted lines: streamlines computed numerically for the same injection points. (b) Numerical (lines) and experimental (symbols) variation of the fluid velocity v along streamlines corresponding to three injection points located at $x = 0$ and $y_{inlet} = 4.5 \pm 1.5$ mm (○, dashed line), 13.5 ± 2.0 mm (△, continuous line), and 21.5 ± 2.0 mm (□, dotted line). The characteristic velocity U upstream of the obstacle is equal to 230 mm s^{-1}. Note that the horizontal and vertical length scales in Fig. (a) are different.

III. EXPERIMENTAL RESULTS

A. Characterization of the flow field

Prior to the injection of the fibers, we have studied the flow velocity variations along the streamlines starting at each of the three selected injection points. Experimentally, a stationary flow is first established in the cell and a stream of dye is then injected at each location (Fig. 2(a)). The progression of the dye is recorded and analyzed using the procedure described in Sec. II. The tip of the dye streak moves at the maximum of the local Poiseuille profile in the gap: this allows one to measure quantitatively the variation of this maximum along the corresponding streamline. The results obtained from these measurements are then compared to those of the $3D$ numerical simulations.

Figs. 2(a)–2(b) show that the experimental and numerical results are in good agreement for both the geometry of the streamlines (a) and the variations of the fluid velocity along them (b). For the most distant streamlines (dotted line and squares in Fig. 2), the velocity increases continuously with distance along x in direct relation with the decrease of the flow section. The results are different for the two other streamlines: the velocity first drops as the fluid reaches the vicinity of the step, then it increases sharply, reaches a maximum right after the step, and decreases finally towards a constant value. Localized buckling may therefore occur in these small regions of decreasing velocity.

Fig. 2 corresponds to an upstream velocity $U = 230$ mm s^{-1} (in the mid-plane between the walls): these numerical simulations were also performed for a velocity 10 times lower. As expected from the Hele Shaw approximation, the streamlines of interest at both velocities (and their curvature) are identical within experimental error while the velocity components are everywhere proportional to U.

Actually, the deformations of the fibers are not due to the v velocity itself but to its spatial variations (see Sec. III D). The variations with the distance x of the normalized gradient components $(\partial v/\partial s)/U$ and $(\partial v/\partial n)/U$ parallel and transverse to the velocity are plotted in Figs. 3(a)–3(b) for the same streamlines as in Fig. 2(b). The parallel component $(\partial v/\partial s)/U$ has its highest positive value (inducing an extensional force) in the region of maximum slope of the streamlines (Fig. 3(a)); it is instead negative (and produces a compressional force which may induce buckling) at the very beginning and end of the steps. The transverse component $(\partial v/\partial n)/U$ which will be seen to induce deformations of the fiber (see Sec. III C) goes instead to zero when the slope of the streamlines is the highest; $(\partial v/\partial n)/U$ reaches its maximum positive and negative values in the regions of maximum curvature (Fig. 3(b)). The width of these extrema is of the order of 30 mm.

Quantitatively, Table II lists the minimal (negative) and maximal values (as determined from the numerical simulations) of the curvature of the line together with the transverse normalized velocity

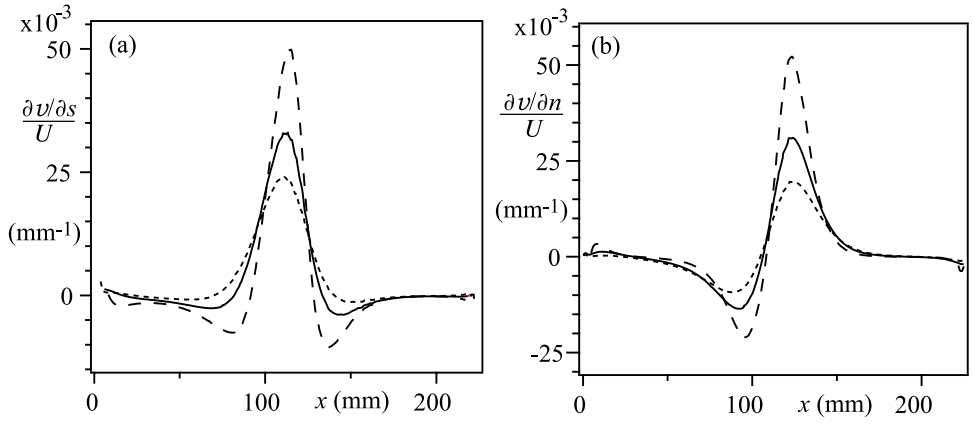

FIG. 3. Variations as a function of the distance x of the normalized parallel and transverse components $(\partial v/\partial s)/U$ (a) and $(\partial v/\partial n)/U$ (b) of the gradient of flow velocity v computed numerically for the same streamlines as in Fig. 2(b) (the different types of lines have the same meaning as in this latter figure).

TABLE II. Transverse coordinate y_{inlet} at inlet, maximum (κ_s^{max}), and minimum (κ_s^{min}) curvatures and velocity gradient $(1/U)(\partial v/\partial n)$ at the corresponding locations for the three streamlines shown in Fig. 2.

Initial location	Maximum curvature (upstream)		Minimum curvature (downstream)	
y_{inlet} (mm)	κ_s^{max} (mm^{-1})	$(1/U)(\partial v/\partial n)$ (mm^{-1})	κ_s^{min} (mm^{-1})	$(1/U)(\partial v/\partial n)$ (mm^{-1})
4.5	0.0144	−0.014	−0.0212	0.039
13.5	0.0109	−0.006	−0.011	0.0222
21.5	0.0077	−0.0034	−0.0066	0.011

gradient $(\partial v/\partial n)/U$ at the same locations; as mentioned above, these values are independent of U. At the distances $x = 90$ and 130 mm corresponding to the minimal and maximal velocities along the streamline closest to the obstacle, one finds, respectively, $(\partial v/\partial n) \sim 0.015\,U$ and $0.04\,U$. The experimental values are very close to the numerical ones.

B. Mean velocity and orientation of the fiber

We have studied the velocity V_f of the center of mass of fibers of diameters $D = 0.49$ and 0.91 mm corresponding to confinement ratios $D/H = 0.22$ and 0.41 and initially straight and parallel to the flow. In the parallel flow region upstream of the step where $v = U$, one finds that $V_f = (0.97 \pm 0.05)U$ and $V_f = (0.87 \pm 0.1)U$. The ratio V_f/U only depends on the diameter of the fibers and not of their length. Moreover, from Fig. 4(a), the velocity V_f remains close to v at all distances along the streamline and not only in its parallel part. These results agree with an experimental and numerical study by other authors[25] of the transport of rigid fibers by a Poiseuille flow between parallel flat walls. For the same ratios $D/H = 0.22$ and 0.41, these authors predict that V_f is, respectively, only 4% and 10% lower than v. V_f is, in addition, the same for fibers parallel and perpendicular to the flow. This small difference between V_f and v, particularly for $D/H = 0.22$, implies that the friction forces due to the relative motion of the fiber and the walls do not play a major part in the phenomenon. The velocity of the fluid in the center part of the cell gap is, therefore, used as the relevant velocity of the problem.

As the fiber moves along the streamline, it becomes tilted with respect to the vertical axis x as it moves over the step: the variations of the tilt angle θ_f with the distance x for the three streamlines are plotted in Fig. 4, together with those of the local tilt angle θ_s of the streamline at the same distance. The variations of θ_f and θ_s are very similar, particularly for the two streamlines farthest from the contour of the step. For that closest to the contour, instead, the maximum tilt angle of the fiber is slightly lower than that of the streamline; moreover, θ_f does not revert exactly to zero after

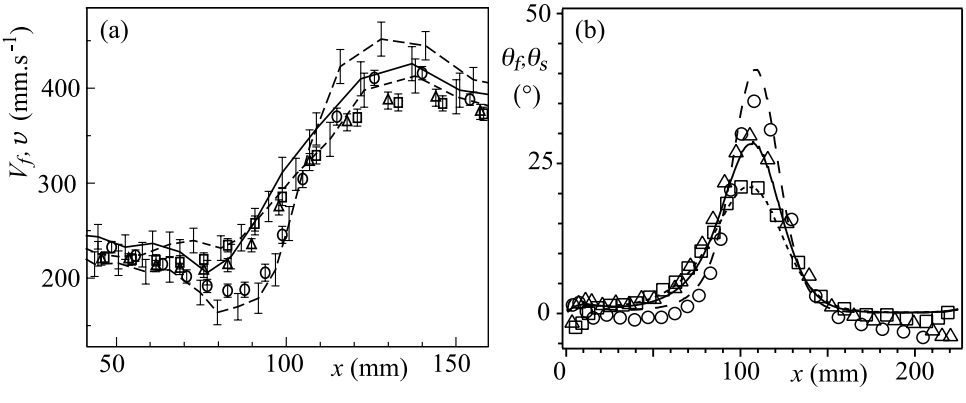

FIG. 4. (a) Experimental variations as a function of the distance x of the flow velocity v measured by the injection of dye (lines) and of the velocity V_f of the center of mass of a 30 mm long fiber of diameter $D = 0.49$ mm (symbols) along streamlines corresponding to the three same injection points as in Fig. 2. (b) Variation as a function of the distance x of the local angles with the axis x of the flow velocity (lines) and of the fiber (symbols). Fluid velocity upstream of the obstacles: $U = 230$ mm s^{-1}. The meaning of the symbols and of the different types of lines is the same as in Fig. 2(b).

the step. This suggests that a part of the fiber moves into the layer close to the contour where the Hele Shaw approximation of zero 2D vorticity in the (x, y) plane is not valid any more, resulting in a residual rotation. When the fiber happens to be injected particularly close to the obstacle, this rotation may be so large that the fiber touches the obstacle; such experiments are not included in the present interpretations.

C. Deformations of fibers of constant length

In this section, we compare the deformations of fibers of same length $L_f = 30$ mm at different distances x on a given streamline and for three different values of the mean flow velocity. Fig. 5 displays superimposed images of fibers of same diameter $D = 0.49$ mm obtained at these different velocities in the regions of maximum positive (a) and negative (b) curvature of two different streamlines (these regions are located, respectively, on the upstream and downstream sides of the step). In case (b), increasing the fluid velocity strongly increases the curvature of the fiber which becomes of the order of that of the streamline: this is particularly visible on the streamline closest to the contour of the step. For the other, the curvature is always similar to that (weaker) of the other streamline. In case (a), the effect of the velocity is still clear close to the contour but much weaker on the other streamline.

These informations are complemented by Fig. 6 displaying the variation with distance of the curvature κ_f of the same fiber as it moves along the streamline corresponding to $y_{inlet} = 13.5$ mm. This variation is compared for different velocities U to that of the local curvature κ_s of the streamline: κ_f reaches extremal values at distances x close to those corresponding to the extrema κ_s^{max} and κ_s^{min}. The minimum of κ_f downstream of the obstacle is of the order of the minimum value of κ_s at all velocities while it is significantly lower and increases with U for the maximum upstream. Up to the end of the step, the curvatures of the fiber and of the streamline follow a similar trend of variation with the distance x, even though the amplitudes are generally different. Farther downstream and at the highest velocity, the curvature of the fiber displays a second maximum while that of the streamline returns to zero. This may be due to buckling induced by the locally negative value of the derivative $\partial v/\partial s$ shown in Fig. 3(a) and resulting in a compressional stress on the fiber just downstream of the step. Figs. 5 and 6 both show, therefore, that the absolute curvature of the fiber increases with the local curvature of the streamlines but depends also of the local flow.

We study now quantitatively the values of these extremal curvatures at different flow rates. Since the flow is laminar, the curvature of the fibers corresponds to a balance between elastic and viscous forces: the latter are induced by *local* velocity differences between different parts of the fiber and the fluid. These differences are small compared to the characteristic flow velocity U since the *global* fiber velocity is close to that of the fluid: the corresponding Reynolds number is also

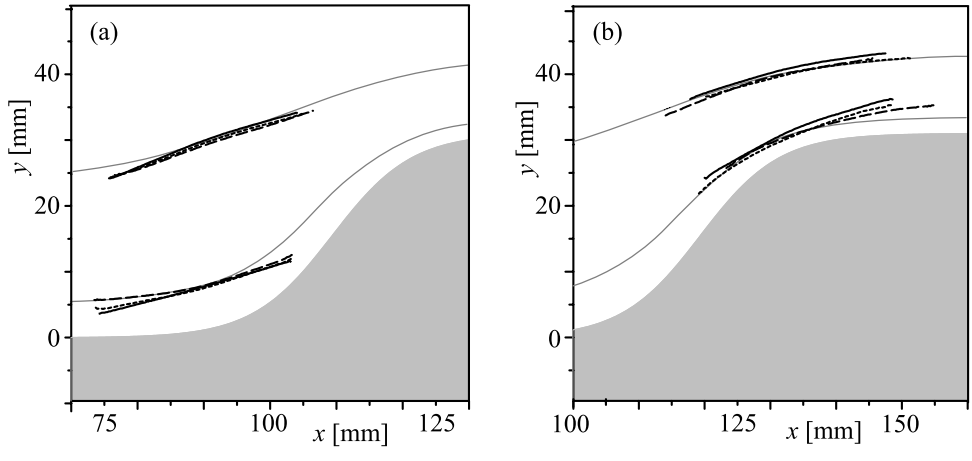

FIG. 5. Fibers ($L_f = 30$ mm, $D = 0.49$ mm) observed at two particular locations upstream (left) and downstream (right) of the step for three upstream velocities: $U = 95$ mm s^{-1} (black), 160 mm s^{-1} (light gray), and 230 mm s^{-1} (gray). Streamlines correspond to $y_{inlet} = 4.5$ mm (dashed line) and $y_{inlet} = 21.5$ mm (dotted line). Fluid viscosity: $\mu = 15$ mPa s.

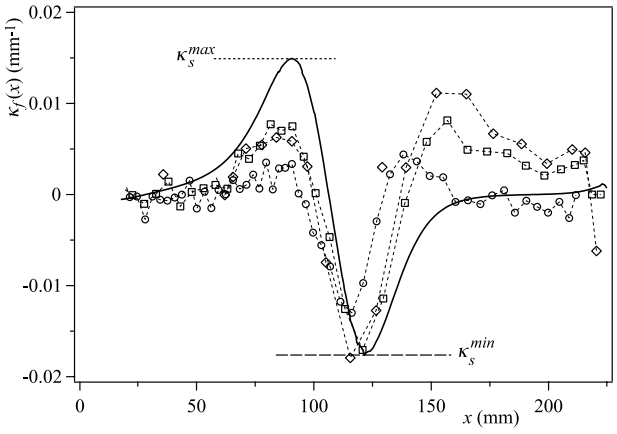

FIG. 6. Curvature κ_f (mm^{-1}) of a fiber ($D = 0.49$ mm, $L_f = 30$ mm) as a function of the coordinate x of its geometrical center for an initial location $y_{inlet} = 13.5$ mm and for flow velocities: (○) $U = 95$, (□) 168, and (◇) 230 mm s^{-1}. Continuous line: curvature of the corresponding streamline at the same distance. Fluid viscosity: $\mu = 15$ mPa s. κ_s^{max}, κ_s^{min}: maximum and minimum curvatures of the streamlines.

small and the viscous stresses are proportional to these velocity contrasts. The relation of the latter to the spatial variations of the velocity and the deformation of the fiber and the streamlines is discussed in Sec. III D but, as a first step, $\mu\,\partial v/\partial n$ will be chosen as the reference viscous stress: $\partial v/\partial n$ is indeed strongly correlated to the variations of the curvature, as shown by Figs. 3 and 6.

Fig. 7 displays variations of κ_f/κ_s as a function of the viscous stress $\mu\,\partial v/\partial n$ (κ_f/κ_s is used as the parameter of interest since, from Fig. 6, one has always $\kappa_f \leq \kappa_s$). Significant curvatures κ_f/κ_s are only observed for the water-glycerol solution (viscous stresses are too low for water (✳ symbols)). As expected, for a given $\mu\,\partial v/\partial n$, the curvatures are also the highest for the most flexible fiber ($D = 0.49$ mm). In this latter case (□ symbols), κ_f/κ_s increases at first linearly with $\mu\,\partial v/\partial n$ and then tends toward a limit of the order of 1 (the fiber coincides locally with the streamline). This limit is not reached for the less flexible fibers (○ symbols).

D. Characteristic dimensionless number

In order to collapse the data corresponding to different fibers onto a single master curve, it is necessary to replace as the horizontal scale $\mu(\partial v/\partial n)$ by a combination including, in addition, the diameter and the length of the cylinder and the stiffness of its material. As mentioned above, the

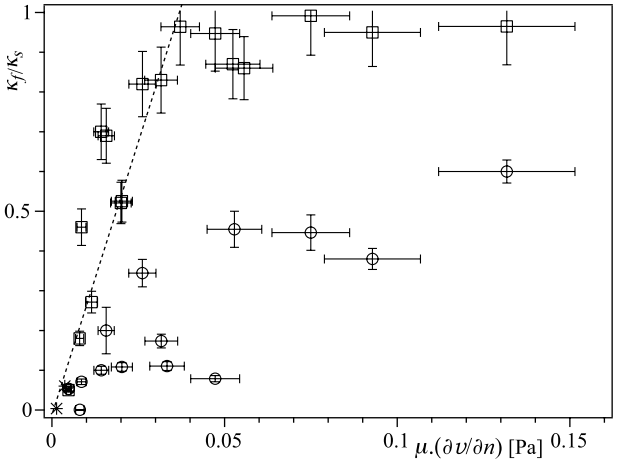

FIG. 7. Dimensionless curvature, κ_f/κ_s, of fibers of length $L_f = 30$ mm as a function of the viscous stress $\mu(\partial v/\partial n)$. Diameter $D = 0.49$ mm; (□): viscosity $\mu = 15$ mPa s, (✳): $\mu = 1$ mPa s. (○): $D = 0.91$ mm, $\mu = 15$ mPa s.

degree of bending of the fiber reflects a balance between the viscous and elastic forces upon it. The value of the diameter influence both of them:

- The curvature κ_f of a fiber of length L_f submitted to a force q per unit length scales as $qL_f^2/(E\,I)$: $E\,I$ is the bending modulus with $I = \pi D^4/64$. The force necessary to achieve a given curvature scales therefore as D^4.
- In the present case, q is a viscous stress associated to the local relative velocity. q also depends on D through the confinement ratio D/H: Increasing D/H results indeed in a stronger blockage of the flow normal to the fiber and, thus, enhances the normal viscous stress. This confinement effect is taken into account by introducing a factor $\lambda_p^\perp(D/H)$ in the proportionality relation between the viscous stress and both the relative velocity of the fiber and the fluid and the viscosity of the latter. The influence of D/H on the force on fixed circular cylinders in a similar flow geometry has been studied in Refs. 26–28. For the ratios $D/H = 0.22$ and 0.41 corresponding to $D = 0.49$ and 0.91 mm, these studies provide respective values $\lambda_p^\perp = 30$ and 73.

As suggested in Sec. III C, the viscous forces are proportional to the local relative velocities of the different parts of the cylinders and the fluid in the regions where the streamlines are curved. These relative velocities may be estimated by multiplying $\partial v/\partial n$ by the local distance between the ends of the fiber (of curvature κ_f) and a streamline of curvature κ_s: this distance is then of the order of $(\kappa_s - \kappa_f)L_f^2$ so that we take $q \propto \lambda_p^\perp \mu(\kappa_s - \kappa_f)L_f^2(\partial v/\partial n)$. The factor $\lambda_p^\perp$ takes into account the confinement of the flow. Using this expression in the estimation of the curvature κ_f leads to

$$\frac{\kappa_f}{\kappa_s - \kappa_f} = CSp = C\frac{\lambda_p^\perp \mu L_f^4(\partial v/\partial n)}{E\,I}. \tag{2}$$

The right hand side of the equation is the Sperm number Sp defined by Eq. (1) with the additional factor $\lambda_p^\perp$.

Fig. 8 shows the variation of κ_f/κ_s as a function of Sp. This time, the data corresponding to the two different fiber diameters collapse onto a same global trend. At low values of $Sp \ll 100$, the ratio κ_f/κ_s increases steeply with Sp ($\kappa_f/\kappa_s \simeq Sp/110$ for the dashed line). At large values of $Sp \gtrsim 500$, κ_f/κ_s becomes of the order of 1 and the profile of the fiber follows the streamlines. The dashed line corresponds to the best fit of these experimental data by Eq. (2) which is obtained for $C = 1/110$ so that $\kappa_f/\kappa_s = Sp/(110 + Sp)$: the fitted curve follows well the trend of the experimental data.

Two of the data points plotted in Fig. 8 correspond to the lower viscosity $\mu = 1$ mPa s. Like in Fig. 7 (and for the same reasons), the corresponding values of κ_f/κ_s are significantly lower.

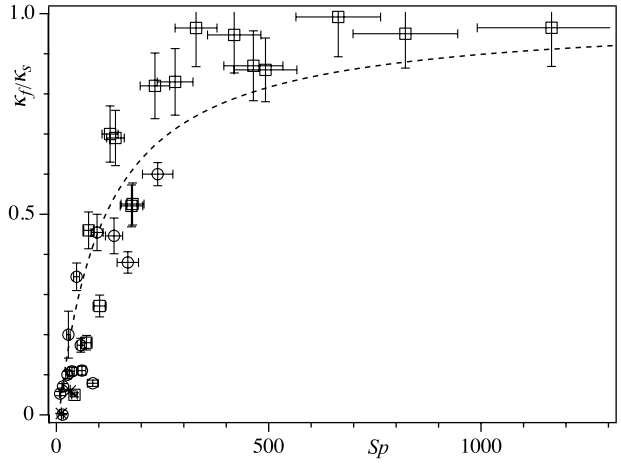

FIG. 8. Dimensionless curvature, κ_f/κ_s of fibers of constant length: $L_f = 30$ mm as a function of the Sperm number $Sp = \lambda_p^\perp \mu(\partial v/\partial n)L_f^4/EI$. Fiber diameter: $D = 0.49$ mm (□, ∗), $D = 0.91$ mm (○); fluid viscosity: $\mu = 15$ mPa s (○, □), $\mu = 1$ mPa s (∗). Dashed line: predictions from Eq. (2) with $C = 1/110$.

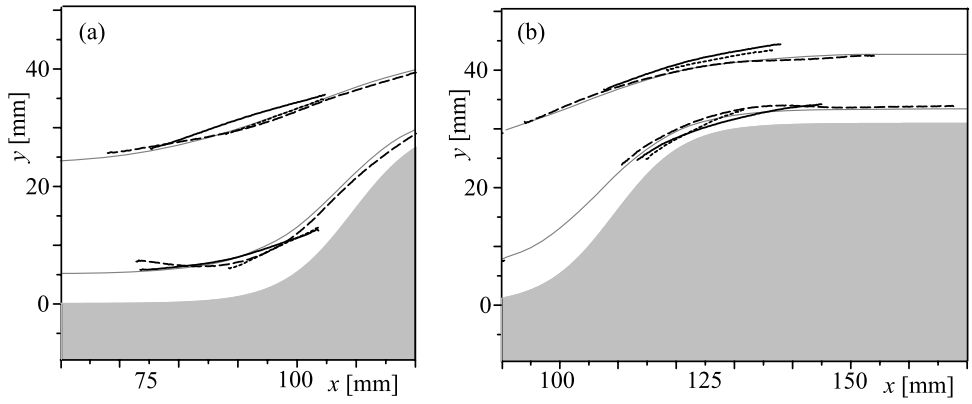

FIG. 9. Superimposition of fibers of different lengths L_f = 15 (dotted lines), 30 (continuous lines), and 60 mm (dashed lines) over two streamlines (thin grey lines) at two locations upstream (left) and downstream (right) of the step. Fluid velocity: U = 230 mm s^{-1}; transverse locations of injection point: y_{inlet} = 4.5 and 21.5 mm.

E. Influence of the length of the fiber

All the experiments described above were performed with fibers of length L_f = 30 mm. Further measurements of the curvature and longitudinal velocity have been performed both for shorter and longer fibers (Fig. 9): increasing the length L_f increases indeed the normal viscous stress ($\propto L_f^2$) while it reduces the elastic force needed for a given bending ($\propto L_f^{-2}$). In agreement with Eq. (2), κ_f/κ_s should then scale like L_f^4 while it is $\ll 1$.

Fig. 9 displays the shapes of fibers of different lengths carried over the obstacle by a flow of given velocity and viscosity. While the curvature decreases clearly as L_f drops from 30 to 15 mm, its value for the longest fiber (L_f = 60 mm) is similar to that for L_f = 30 mm. As seen in Fig. 6, bending is indeed localized to the regions of maximum curvature of the streamlines. Therefore, for L_f = 60 mm, only a fraction of the length of the fiber is exposed to a large normal viscous stress: this exposed length is of the order of the width $\Delta W \simeq$ 30 mm of each extremum of $\partial v/\partial n$ in the curves of Fig. 3(b) and is independent of L_f. For long fibers ($L_f \gtrsim \Delta W$), the relevant length to be used in the expression of Sp is therefore ΔW instead of L_f. For this reason, we replace the expression of Sp from Eq. (2) by the more general expression

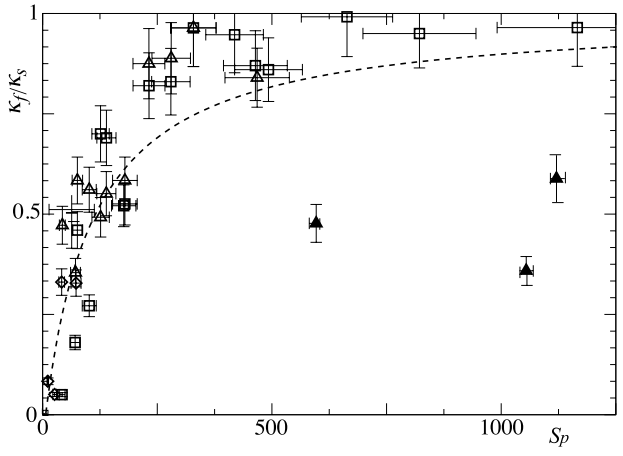

FIG. 10. Dimensionless curvature κ_f/κ_s as a function of Sp for different lengths of the fibers: L_f = 15 mm ((◊) D = 0.49 mm), L_f = 30 mm ((○) D = 0.49 mm, (□) D = 0.91 mm), and L_f = 60 mm (D = 0.91 mm) with ΔW (△) and L_f (▲) as the characteristic length in the definition of Sp. Fluid viscosity: μ = 15 mPa s. Dashed line: predictions from Eq. (2) with a proportionality factor 1/110.

$$Sp = \frac{\lambda_p^{\perp}\,\mu\,\xi^4(\partial v/\partial n)}{E\,I}, \tag{3}$$

in which $\xi = L_f$ for $L_f \le \Delta W$ and $\xi = \Delta W$ for $L_f \ge \Delta W$. The validity of these assumptions is tested in Fig. 10 displaying the variation of κ_f/κ_s with Sp for fibers of different lengths and diameters. For the two shortest fibers $L_f = 15$ and $L_f = 30$ mm, one has $L_f \le \Delta W$ so that both definitions of Sp are valid; for $L_f = 60$ mm, a better collapse is clearly obtained by using the definition of Sp from Eq. (3) ($\triangle$) than from Eq. (2).

IV. DISCUSSION AND CONCLUSION

The present experiments identified the parameters controlling the motion and deformation of a flexible fiber in a confined Hele-Shaw flow where a step-like obstacle induces variations of the magnitude and orientation of the velocity.

Both the trajectory of the center of mass of the fiber and its orientation follow globally those of the corresponding streamline. This contrasts with pinned flexible fibers or fibers placed in a Poiseuille flow, for which the fibers may cross the streamlines. Moreover, the velocity of the fibers is proportional to the fluid velocity at their center of mass with a constant only depending of the geometrical confinement. The variations of the curvature κ_f of the fiber also follow closely those κ_s of the streamlines but, generally, with a smaller amplitude.

Quantitatively, a key result of the present study is that the normalized curvature κ_f/κ_s of the fibers is only a function of a combination Sp (the Sperm number) of different parameters of the flow given by Eq. (3). Physically, relation (2) between κ_f/κ_s and Sp reflects the balance between viscous forces applied by the flowing fluid on the fiber and elastic forces opposing the resulting deformations. The viscous forces are proportional to the transverse velocity gradient, to the local distance between the fiber and the streamline and to the fluid viscosity. The elastic restoring forces, per unit length, are proportional to the curvature of the fiber, to its bending stiffness $E\,I \propto D^4$ and vary as ξ^{-2} with its effective length ξ for a given curvature: ξ coincides with the length L_f only for short fibers. For longer ones, ξ must be taken equal in the expression of Sp to a characteristic length of the variation of the flow. Here, if $L_f \ge \Delta W$, ξ is equal to the width ΔW of the region where the component $\partial v/\partial n$ of the gradient of the velocity is large (Fig. 3(b)); parts of the fibers outside this region do not influence bending.

In contrast with many previous studies of the dynamics of flexible fibers, one deals here with a confined configuration of a fiber between two parallel walls; this keeps the motion of the fiber bi-dimensional and enhances the viscous forces due to the partial blockage of the flow; this effect is taken care of by introducing a dimensionless parameter $\lambda_p^{\perp}$ depending on the diameter. The diameter influences, however, bending mainly through the D^4 factor in EI which increases the rigidity considerably and reduces bending for fibers of larger diameter.

The present study can be applied to the transport of flexible fibers in fractures containing obstacles occupying a part of the area: the quantitative information we obtained can be transposed to estimate the influence of the length and diameter of the fibers, of the fracture gap and the size in the fracture plane of the obstacles (modeled here as step reducing the width of an Hele-Shaw cell).

In the present flow geometry, the velocity of the flow increases with distance which keeps the fiber under tension, except in localized regions. It will be important to investigate the opposite case in which buckling may, for instance, occur. The discussion presented above is largely based on a local balance between elastic and viscous forces. Nonlocal effects might, however, occur for fibers submitted to a sequence of variations of curvatures of the streamlines over distances smaller than their length. Interactions between the different parts of the fiber may then be significant: this may have an important influence on transport in porous media or micro-fluidic circuits.

ACKNOWLEDGMENTS

We acknowledge support by the RTRA Triangle de la Physique and the LIA PMF-FMF (Franco-Argentinian International Associated Laboratory in the Physics and Mechanics of Fluids).

We thank R. Pidoux for the realization of the experimental cell. We are grateful to G. Kasperski for his help with the numerical simulations of the flow field.

[1] K. Yasuda, T. Kyuto, and N. Mori, "An experimental study of flow-induced fiber orientation and concentration distributions in a concentrated suspension flow through a slit channel containing a cylinder," Rheol. Acta **43**, 137-145 (2004).
[2] A.-K. Tornberg and K. Gustavsson, "A numerical method for simulations of rigid fiber suspensions," J. Comput. Phys. **215**, 172-196 (2006).
[3] P. R. Howard, M. T. King, M. Morris, J.-P. Feraud, G. Slusher, and S. Lipari, "Fiber/proppant mixtures control proppant flowback in South Texas," SPE Annual Technical Conference and Exhibition, Dallas, TX, 22-25 October 1995 (Society of Petroleum Engineers, 1995), pp. 453-454.
[4] E. M. Purcell, "Life at low Reynolds number," Am. J. Phys. **45**, 3-11 (1977).
[5] E. Lauga and T. R. Powers, "The hydrodynamics of swimming microorganisms," Rep. Prog. Phys. **72**, 096601 (2009).
[6] M. C. Lagomarsino, F. Capuani, and C. P. Lowe, "A simulation study of the dynamics of a driven filament in an Aristotelian fluid," J. Theor. Biol. **224**, 215-224 (2003).
[7] M. C. Lagomarsino, I. Pagonabarraga, and C. Lowe, "Hydrodynamic induced deformation and orientation of a microscopic elastic filament," Phys. Rev. Lett. **94**, 148104 (2005).
[8] R. Chelakkot, R. G. Winkler, and G. Gompper, "Migration of semiflexible polymers in microcapillary flow," Europhys. Lett. **91**, 14001 (2010).
[9] S. Reddig and H. Stark, "Cross-streamline migration of a semiflexible polymer in a pressure driven flow," J. Chem. Phys. **135**, 165101 (2011).
[10] A. M. Slowicka, M. L. Ekiel-Jezewska, K. Sadlej, and E. Wajnryb, "Dynamics of fibers in a wide microchannel," J. Chem. Phys. **136**, 044904 (2012).
[11] R. Rusconi, S. Lecuyer, L. Guglielmini, and H. A. Stone, "Laminar flow around corners triggers the formation of biofilm streamers," J. R. Soc., Interface **7**, 1293-1299 (2010).
[12] M. D'Angelo, B. Semin, G. Picard, M. Poitzsch, J.-P. Hulin, and H. Auradou, "Single fiber transport in a fracture slit: Influence of the wall roughness and of the fiber flexibility," Transp. Porous Media **84**, 389-408 (2010).
[13] O. L. Forgacs and S. G. Mason, "Particle motions in sheared suspensions: X. Orbits of flexible threadlike particles," J. Colloid Interface Sci. **14**, 473-491 (1959).
[14] J. M. Stockie and S. I. Green, "Simulating the motion of flexible pulp fibers using the immersed. Boundary method," J. Comput. Phys. **147**, 147-165 (1998).
[15] G. Wang, W. Yu, and C. Zhou, "Optimization of the rod chain model to simulate the motions of a long flexible fiber in simple shear flows," Eur. J. Mech. B/Fluids **25**, 337-347 (2006).
[16] S. B. Lindström and T. Uesaka, "Simulation of the motion of flexible fibers in viscous fluid flow," Phys. Fluids **19**, 113307 (2007).
[17] E. Wandersman, N Quennouz, M. Fermigier, A. Lindner, and O. du Roure, "Buckled in translation," Soft matter **6**, 5715-5719 (2010).
[18] Y. N. Young and M. J. Shelley, "Stretch-coil transition and transport of fibers in cellular flows," Phys. Rev. Lett. **99**, 058303 (2007).
[19] L. Guglielmini, A. Kushwaha, E. S. G. Shaqfeh, and H. A. Stone, "Buckling transitions of an elastic filament in a viscous stagnation point flow," Phys. Fluids **24**, 123601 (2012).
[20] V. Kantsler and R. E. Goldstein, "Fluctuations, dynamics, and the Stretch-Coil transition of single actin filaments in extensional flows," Phys. Rev. Lett. **108**, 038103 (2012).
[21] N. Autrusson, L. Guglielmini, S. Lecuyer, R. Rusconi, and H. A. Stone, "The shape of an elastic filament in a two-dimensional corner flow," Phys. Fluids **23**, 063602 (2011).
[22] J. S. Wexler, P. H. Trinh, H. Berthet, N. Quennouz, O. du Roure, H. E. Huppert, A. Lindner, and H. A. Stone, "Bending of elastic fibres in viscous flows: The influence of confinement," J. Fluid Mech. **720**, 517-544 (2013).
[23] M. Habibi, N. M. Ribe, and D. Bonn, "Coiling of elastic ropes," Phys. Rev. Lett. **99**, 154302 (2007).
[24] B. Semin, H. Auradou, and M. Françis, "Accurate measurement of curvilinear shapes by virtual image correlation," Eur. Phys. J. App. Phys. **56**, 10701 (2011).
[25] H. Berthet, M. Fermigier, and A. Lindner, "Single fiber transport in a confined channel: Microfluidic experiments and numerical study," Phys. Fluids **25**, 103601 (2013).
[26] A. Ben Richou, A. Ambari, and J. K. Naciri, "Drag force on a circular cylinder midway between two parallel plates at very low Reynolds numbers. Part 1: Poiseuille flow (numerical)," Chem. Eng. Sci. **59**, 3215-3222 (2004).
[27] A. Ben Richou, A. Ambari, M. Lebey, and J. K. Naciri, "Drag force on a cylinder midway between two parallel plates at $Re \ll 1$ Part 2: Moving uniformly (numerical and experimental)," Chem. Eng. Sci. **60**, 2535-2543 (2005).
[28] B. Semin, J.-P. Hulin, and H. Auradou, "Influence of flow confinement on the drag force on a static cylinder," Phys. Fluids **21**, 103604 (2009).